8B.2

MULTISCALE OBSERVATIONS OF TROPICAL CYCLONE STRUCTURE USING AIRBORNE DOPPLER COMPOSITES

Robert Rogers[1], Sylvie Lorsolo[2], Paul Reasor[1], John Gamache[1], Frank Marks[1]

[1]NOAA/AOML Hurricane Research Division (HRD)
Miami, FL

[2]Univ. of Miami/Cooperative Institute for Marine and Atmospheric Studies (CIMAS)
Miami, FL

1. INTRODUCTION

The multiscale nature of the processes governing tropical cyclone (TC) intensity and structure is a major reason why advances in TC intensity forecasts lag advances in track forecasts. These processes range in scale from environmental scale to vortex, convective, turbulent, and microscales, with spatial scales ranging from O(1000 km) to O(1 mm). A better understanding and modeling of these processes, and the upscale and downscale interactions among them, is necessary before significant forecast improvements can be realized. Observations across these scales play an important role in this task, both in improving our understanding of the relevant physical processes and the modeling of them through rigorous data assimilation and detailed model evaluation.

Airborne Doppler radar data is a key dataset for observing the vortex- and convective-scale structure and evolution of TCs. Studies of individual cases using NOAA airborne Doppler radar have documented many aspects of both the symmetric and asymmetric vortex- and convective-scale structure and evolution (e.g., Jorgensen 1984, Marks and Houze 1987, Houze et al. 1992, Gamache et al. 1993, Dodge et al. 1999, Reasor et al. 2000, 2005, 2009). Composites can be helpful for applying these conclusions to a broad set of situations to perform analyses where observations from an individual case may be insufficient. Such composite studies have revealed important characteristics of TC structure and evolution using a variety of datasets, including flight-level (e.g., Shea and Gray 1973, Gray and Shea 1973, Kossin and Eastin 2001), GPS dropsonde (e.g., Franklin et al. 2003), and rawinsonde data (e.g., Frank 1983).

Composites of airborne Doppler data, collected by the NOAA Hurricane Research Division (HRD) for the past 30 years, can provide information on three-dimensional TC inner-core structures in a statistically robust framework. Multiple applications are possible using this compositing methodology that complements well the case study approach. The purpose of this work is to demonstrate the utility of calculating composites of inner-core TC structure across multiple scales from a multitude of TCs using airborne Doppler data.

Corresponding author address: Robert Rogers, NOAA/AOML Hurricane Research Division, Robert.Rogers@noaa.gov

2. METHODOLOGY

Composites of inner-core structure are calculated using tail Doppler radar data from NOAA WP-3D radial penetrations in multiple storms from 1997 to 2008. A total of 19 radial penetrations from seven different storms during this time period are included in the composite (Table 1). All of the storms were of at least Category 3 intensity on the Saffir-Simpson scale. Several storms, including Hurricanes Isabel, Katrina, and Rita, were Category 5 at the time of the radar sampling.

Storm name	Date (mm/dd/yyyy)	Number of analyses	best track intensity at time of radar analysis (kt)
Frances	9/1/2004	3	120
Guillermo	8/2/1997	2	105
Isabel	9/12/2003	3	140
Isabel	9/14/2003	2	140
Katrina	8/28/2005	4	150
Rita	9/21/2005	3	145
Fabian	9/3/2003	1	110
Paloma	11/8/2008	1	125

Table 1. List of storms used in Doppler composite. Intensity of storm (from Best Track) at time of radar legs included.

A variational analysis (Gamache 1997) of reflectivity and aircraft-relative flow is used to generate 3-D Cartesian grids (swaths) and 2-D profiles of winds and reflectivity above and below the aircraft (see example in Fig. 1). This automated analysis is a global 3-D variational solution of the continuity and Doppler projection equations, similar to that done in Gao et al. (1999) and Reasor et al. (2009) and used in Stern and Nolan (2009). There are several differences in the swath and profile

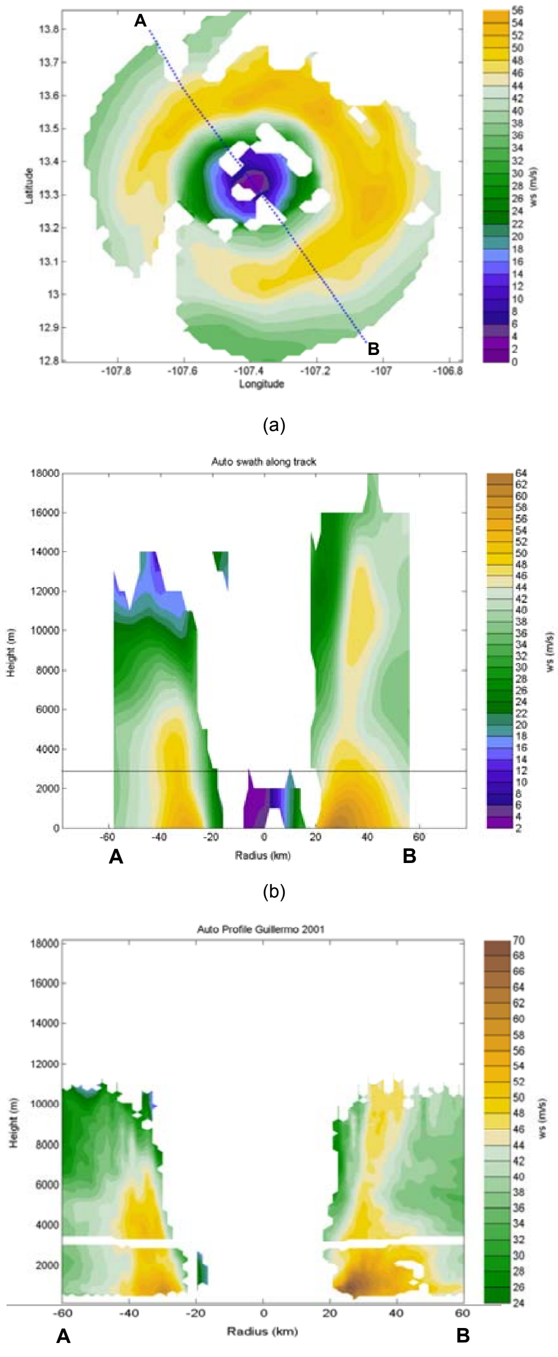

Figure 1. Example of radar analyses used in composites. (a) Wind speed (m s^{-1}) at 3 km altitude for 8/2/1997 from Hurricane Guillermo. Line AB denotes location of cross sections of wind sped in (b) and (c); (b) cross section of wind speed (m s^{-1}) produced from swath analysis; (c) as in (b), but for profile analysis.

analyses. One significant difference is the way that vertical velocity is calculated. The swath analysis estimates winds in all three dimensions by solving the continuity equation globally, after subtracting the component along the Doppler radial of the estimated fall speed of the hydrometeors. The profile analysis estimates vertical velocity solely by subtracting the estimated fall speed from the overdetermined precipitation-motion solution (i.e., with no need for continuity constraint). Another difference is the resolution of the data. The swath data has a horizontal grid spacing of 2x2 km and a vertical spacing of 0.5 km. The profile data is calculated by averaging data above and below the aircraft in a 10-km wide region normal to the aircraft track. It produces a 2-D field of winds and reflectivity, with an along-track spacing of 1.5 km and a vertical spacing of 0.15 km.

To calculate several parameters related to the symmetric structure of the storm composites, the Cartesian data from the swaths are interpolated to cylindrical coordinates. The storm center is defined using a simplex algorithm (Neldar and Mean 1965), similar to what has been done for airborne and ground-based radar and numerical modeling studies of TCs (e.g., Marks et al. 1992, Lee and Marks 2000, Rogers et al. 2003). Since different storms are of different sizes, it is necessary to map the radial legs onto a normalized coordinate system in order to perform the composites. This is done by calculating a normalized radius and plotting all relevant fields as a function of this normalized radius. The normalized radius r^* is defined by $r^* = r/r_{max}$, where r_{max} is the radius of maximum axisymmetric wind.

3. RESULTS

a) Summary statistics of structure

Summary statistics of the vortex properties from the 19 radar legs are shown in Table 2. The average radius of maximum axisymmetric wind at 2-km altitude is 30.5 km, with a minimum of 16 km (Paloma on 11/8/08) and a maximum of 40 km (Frances on 9/1/04 and Isabel on 9/14/03). The eyewall slope, defined as the difference between the

	min	max	mean	st dev
RMW_{2km} (km)	16	40	30.5	6.3
2-8 km eyewall slope (km)	-2	8	3.9	2.7
2-8 km center displacement (km)	1.27	10.9	4.17	2.57

Table 2. Summary statistics of vortex properties from all radar legs.

radius of peak axisymmetric wind at 2 km and 8 km altitude (similar to that done in Stern and Nolan 2009) varies between -2 and 8 km, with a mean value of 3.9 km and a standard deviation of 2.7 km, indicating that on average the eyewall slopes outward with increasing altitude. The mean displacement of the center between 2 and 8 km altitude is 4.17 km, with a minimum displacement of 1.27 km (Rita 9/21/05) and a maximum displacement of 10.9 km (Isabel 9/14/03).

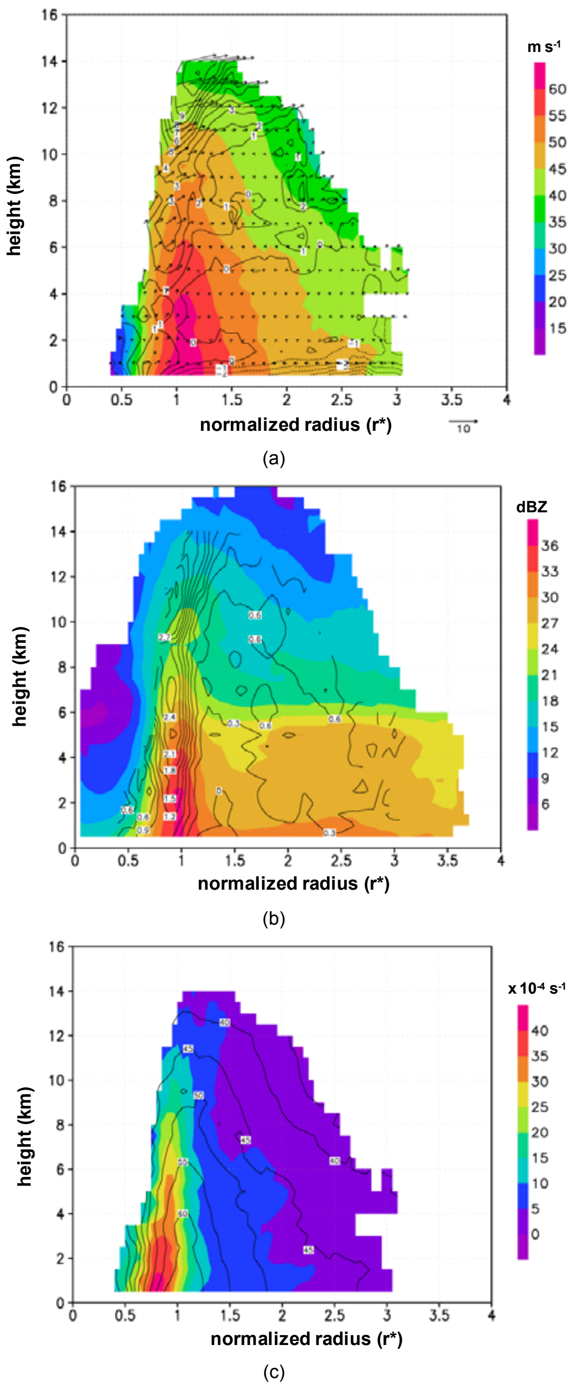

Figure 2. Composite axisymmetric fields obtained from swath data from Table 1, plotted as a function of normalized radius r* and height AGL. Data from a minimum of 10 swaths is required for plotting. (a) tangential (shaded, m s^{-1}) and radial (contoured, m s^{-1}) winds. Vectors of axisymmetric radial and vertical wind (vector, m s^{-1}) also plotted; (b) reflectivity (shaded, dBZ) and vertical velocity (contoured, m s^{-1}); (c) relative vorticity (shaded, x 10^{-4} s^{-1}) and tangential wind (contoured, m s^{-1}).

b) Composite vortex-scale axisymmetric properties

Figure 2 shows radius-height (r*-z) plots of axisymmetric kinematic and reflectivity fields obtained by compositing the swath data obtained from the radar passes shown in Table 1. In order to ensure that an adequate number of swaths comprise the composite, only those areas in r*-z space where data from at least 10 swaths is present are shown here. Many features of the primary and secondary circulation commonly seen in individual case studies (Marks and Houze 1987, Marks et al. 1992) are seen in the composites. Tangential wind, maximized at an r* of 1 with a peak at 1-km altitude that is greater 60 m s^{-1} for this dataset, decreases to 45-50 m s^{-1} by 2*r_{max} and to 40 m s^{-1} by 3*r_{max}. The symmetric radial flow shows inflow as large as 6 m s^{-1} in the lowest 1 km altitude at 2.5*r_{max}. Weak inflow outside r_{max} extends up to 6 km altitude, but the maximum inflow is confined to the lowest 2 km. Outflow occurs along the eyewall, reaching a maximum of 10 m s^{-1} at the 12-km altitude. A shallow region of outflow at the top of the low-level inflow layer is also evident beginning at about 0.75*r_{max} and extending out to about 1.5*r_{max} and below 3 km altitude. Weak outflow is also evident above 6 km altitude extending from 1.5*r_{max} outward. Symmetric reflectivity (Fig. 2b) shows a deep layer associated with the eyewall between 0.75 and 1.25*r_{max}. Outside of that radius is predominantly stratiform-type precipitation, with an area of slightly higher reflectivity below the melting level between 2 and 3*r_{max}, likely associated with rainbands and outer eyewalls that may exist in the dataset. The vertical velocity shows symmetric updrafts reaching a peak near 3 m s^{-1} in the eyewall and weak upward motion at nearly all altitudes outside of the eyewall. The vorticity plot (Fig. 2c) shows vorticity maximized at 40 x 10^{-4} s^{-1} along the inner edge of the eyewall, near 0.75*r_{max}. Inside of that radius the vorticity drops, indicating, in the mean at least, that a ring of vorticity exists for storms from this dataset. Outside r_{max} the vorticity rapidly decreases.

An assessment of the variability of the symmetric structure across storms in the sample is given in Figs. 3 and 4, which show the symmetric vertical velocity and relative vorticity at ±1 standard deviation from the mean. The vertical velocity field at -1 σ maintains the eyewall updraft, albeit weaker than in the mean. One notable difference from the mean field is the presence of a weak downdraft along the outer edge of the eyewall (between 1 and 1.5*r_{max}), and very weak descent elsewhere outside the

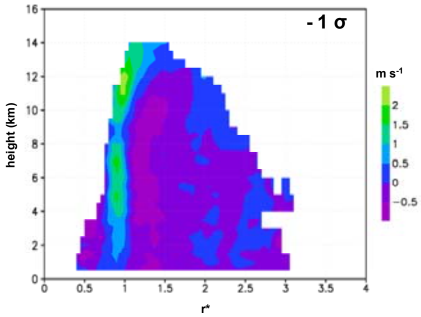

(a)

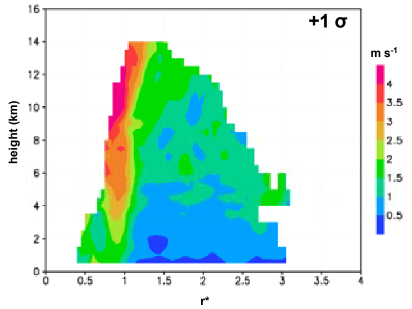

(b)

Figure 3. (a) Composite axisymmetric vertical velocity (shaded, m s^{-1}) one standard deviation below the mean; (b) As in (a), but for one standard deviation above the mean.

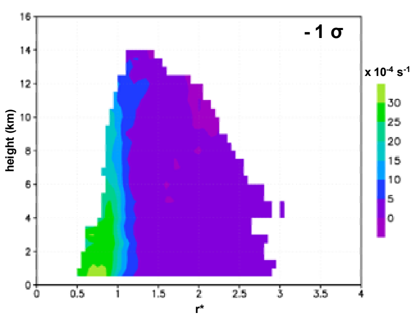

(a)

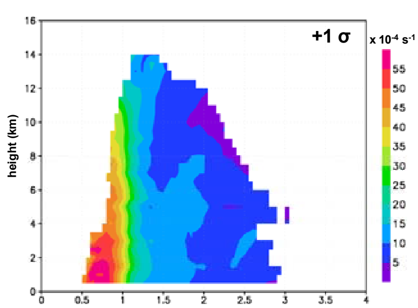

(b)

Figure 4. (a) Composite axisymmetric relative vorticity (shaded, x 10^{-4} s^{-1}) one standard deviation below the mean; (b) As in (a), but for one standard deviation above the mean.

eyewall. For the +1 σ field the eyewall updraft reaches a maximum of 4 m s^{-1} at 10-11 km altitude. Upward motion exists everywhere else throughout the domain. The -1σ vorticity field (Fig. 4a) preserves the peak vorticity along the inner edge of the eyewall and essentially eliminates positive vorticity outside the eyewall. By contrast, the +1σ vorticity field shows a more pronounced vorticity maximum in the low- to mid-troposphere out to 2*r_{max}.

c) Composite convective-scale properties

Statistics of vertical velocity and relative vorticity are calculated from the composites to show the structure of convective-scale features within the composite storm. To examine the radial variation of these parameters the radial dimension is divided into six regions:

Region 1: $r^* < 0.5^*r_{max}$
2: $0.5^*r_{max} \le r^* < 0.75^*r_{max}$
3: $0.75^*r_{max} \le r^* < r_{max}$
4: $r_{max} \le r^* < 1.25^*r_{max}$
5: $1.25^*r_{max} \le r^* < 1.5^*r_{max}$
6: $1.5^*r_{max} \le r^*$

These regions are roughly meant to depict the eye, inner eyewall edge, outer eyewall edge, and outer core.

Figure 5 shows contoured frequency by altitude diagrams (CFADs; Yuter and Houze 1995) of vertical velocity for regions 3 (inner eyewall edge) and 6 (outer core) for all the storms in Table 1. The vertical velocity CFAD for region 3 shows a broad spectrum of updrafts and downdrafts, with peak updraft values reaching 10 m s^{-1} and peak downdrafts of -7 m s^{-1}. The bulk of the distribution (15-30%), though, is found between -1 and 3 m s^{-1}. This pattern is generally consistent with eyewall vertical velocities found in vertical incidence radar data (Black et al. 1996). The CFAD of vertical velocity for region 6 (Fig. 5b) shows a much narrower distribution of vertical velocities, with peak up- and downdrafts of 5 m s^{-1} and 25-30% of the distribution between -1 and 1 m s^{-1}. This distribution is consistent with the Black et al. (1996) vertical incidence measurements for stratiform regions, indicating that this radial region is primarily associated with stratiform processes.

Figure 6 shows CFADs of relative vorticity for these same two regions. The distribution of vorticity along the eyewall inner edge is positively skewed, particularly in the lower troposphere below 4 km. Modal values of vorticity steadily decrease with height, from 4 x 10^{-3} s^{-1} near the surface to 2 x 10^{-3} s^{-1} at 12 km altitude. Peak values of lower-tropospheric vorticity are near 1 x 10^{-2} s^{-1}, while there are very few

(< 0.1%) areas with negative vorticity. Outside of the eyewall, the distribution is again narrower. Peak values reach 4 x 10^{-3} s^{-1}, and there is a sizable portion of the vorticity distribution (>5%) that is negative. The profile also varies little with height.

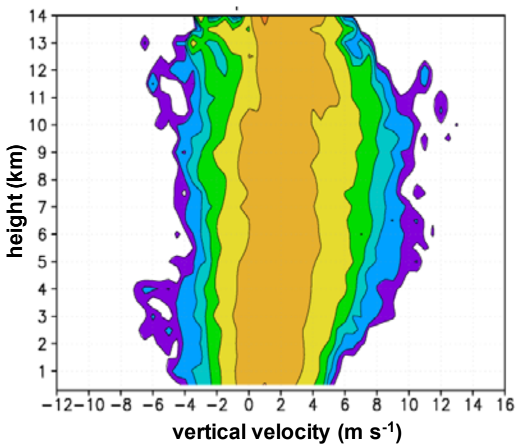

(a)

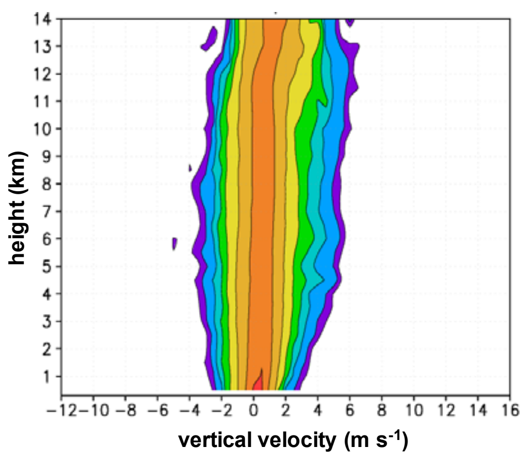

(b)

Figure 5. (a) CFAD of vertical velocity (shaded, %) for region 3; (b) as in (a), but for region 6.

d) Comparison of swath and profile composites

As described earlier, the profile data has several differences in the way it is calculated compared with the swath data, in particular the way in which vertical velocity is calculated and the resolution of the data. Figure 7 shows a comparison of composite radial wind calculated from the swaths and from the profiles. The biggest difference is that the profile composite shows data closer to the surface, 150 m, compared with the minimum altitude of 500 m from the swath data. This proximity to the surface allows the profile composite to capture much stronger low-level inflow, with peak values of -18 m s^{-1} near the surface at an r* between 1 and 1.25 compared with peak inflow values of -6 m s^{-1} in the swath composites. Also, the outflow channel seen just above the inflow layer along the inner edge of the eyewall is better resolved by the profile composite than in the swath composite. These differences are

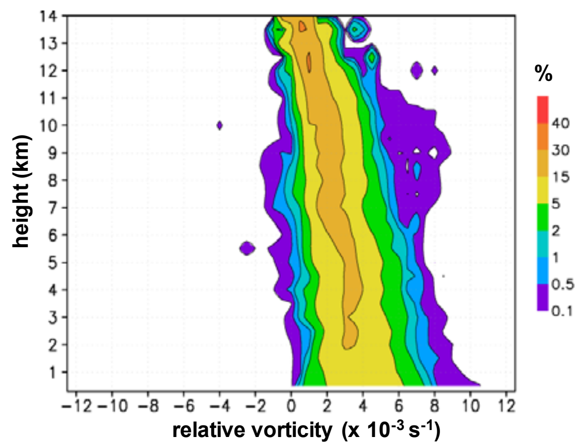

(a)

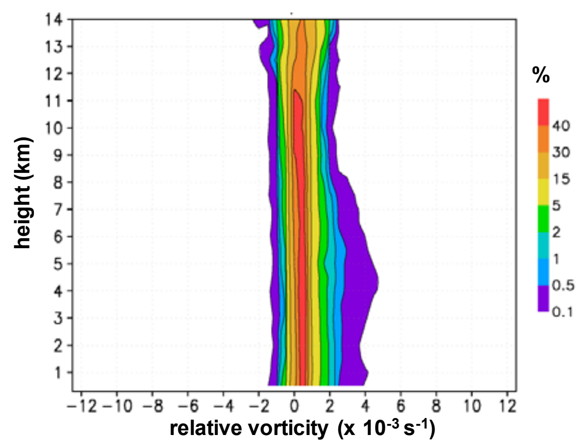

(b)

Figure 6. (a) CFAD of relative vorticity (shaded, %) for region 3; (b) as in (a), but for region 6.

most likely attributable to the different resolutions of the datasets.

Figure 8 shows vertical velocity composites for the swaths and the profiles. Both composites produce the eyewall updraft of comparable peak magnitude (~3 m s^{-1}). However, the altitude of the peak eyewall updrafts varies between the swath and the profiles (> 10 km for the swath, 4 km for the profiles). Outside of the eyewall both the swaths and profiles produce weak ascent in the mid- to upper-troposphere, but the profile data produces more widespread areas of downdrafts of a larger magnitude, including an area of 2 m s^{-1} subsidence just outside the eyewall at 1.25*r_{max}.

CFAD comparisons of vertical velocity from the swath and profile composites for the entire radial domain (Fig. 9) show that, in general, both datasets produce comparable vertical velocity statistics. The most notable differences between the two datasets are a narrower distribution in the lowest 4 km and slightly stronger peak drafts in the profile data. Both datasets compare favorably with the CFAD calculated from the vertical incidence database from Black et al. (1996).

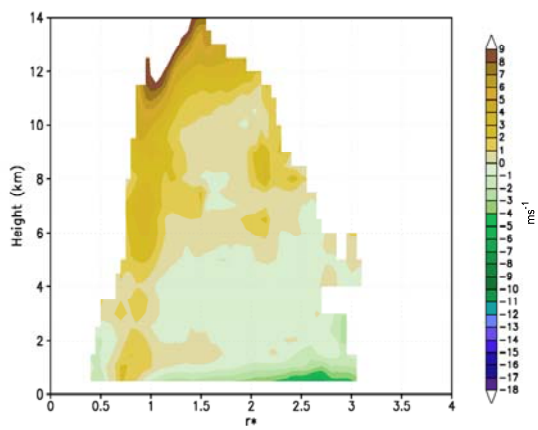

(a)

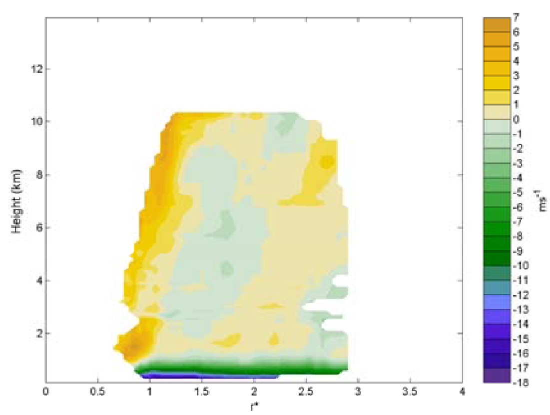

(b)

Figure 7. (a) Composite axisymmetric radial wind (shaded, m s^{-1}) from swath data; (b) as in (a), but for profile data.

Another field that can be calculated from the profile data is turbulent kinetic energy (TKE). Figure 10 shows a composite of TKE for the profile data from the cases shown in Table 1. Two primary regions of maximum TKE are apparent in the composite: in the boundary layer outside of the RMW and within and just along the inner edge of the eyewall. A clear minimum in TKE is evident at radii about $2{*}r_{max}$. This pattern is consistent with the individual and composite fields shown in Lorsolo et al. (2010).

4. SUMMARY AND FUTURE WORK

The airborne Doppler compositing methodology shown here produces many of the structures seen in past case studies, including details of the vortex-scale primary and secondary circulation and distributions of convective- and turbulent-scale

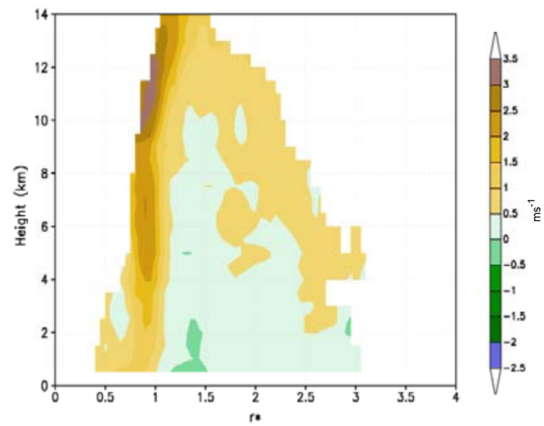

(a)

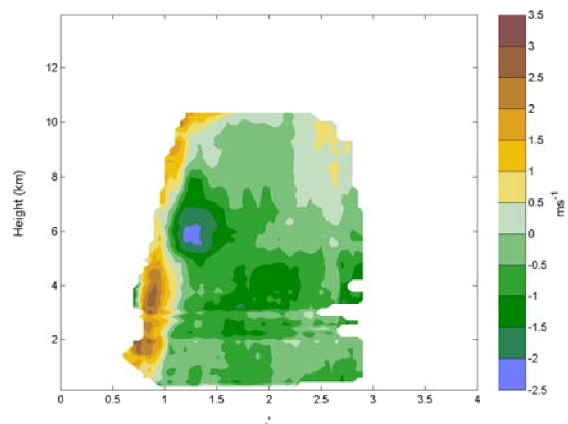

(b)

Figure 8. (a) Composite axisymmetric vertical velocity (shaded, m s^{-1}) from swath data; (b) as in (a), but for profile data.

properties as a function of proximity to the radius of maximum wind. Each of the composites (swath and profile) has its advantages. The swath data produces three-dimensional fields of horizontal and vertical wind and reflectivity. However, vertical resolution is limited, it is limited in how close to the surface it can reliably measure the winds, and there is an additional uncertainty in the vertical velocity calculation that arises from the use of the continuity constraint. The profile data have better vertical resolution and do not have this continuity constraint. As a result they better resolve the low-level inflow and produce much more detail in the vertical velocity fields, especially outside of the eyewall. However, the azimuthal coverage is limited and three-dimensional variables can not be calculated.

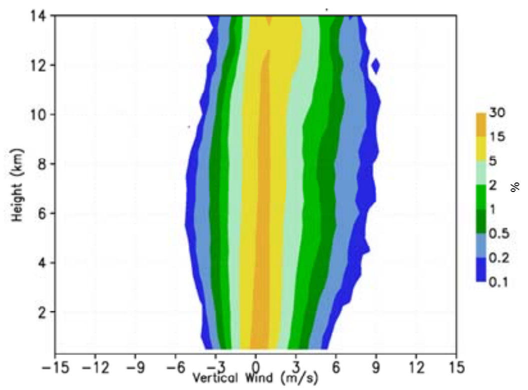

(a)

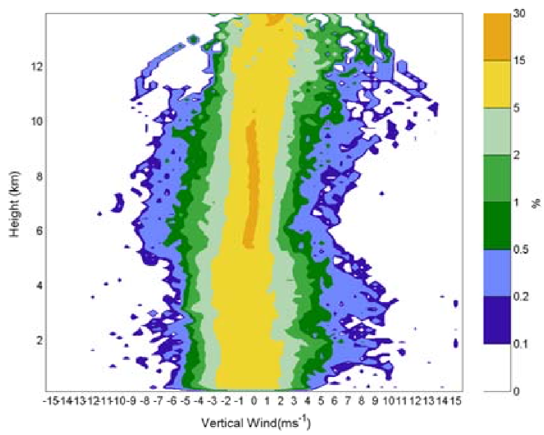

(b)

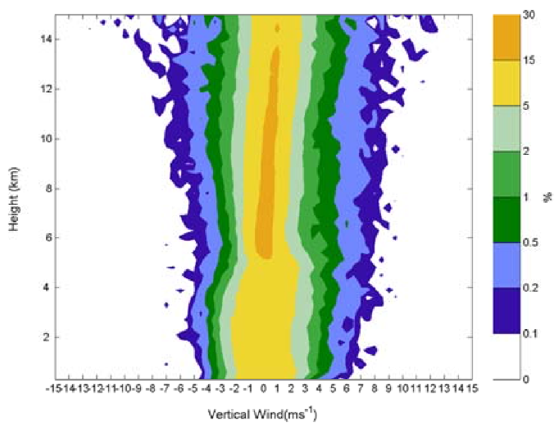

(c)

Figure 9. CFADs of vertical velocity (shaded, %) from entire radial domain for (a) swath data; (b) profile data; (c) vertical incidence dataset from Black et al. (1996).

The use of composites allows for the ability to determine many aspects of the statistical properties of the fields, such the variance of the azimuthal structure around the mean. Whether or not these fields are normally distributed about the mean is a key question to address, and one which can be determined within the composite framework here.

Future work will involve adding more radar analyses to the database. Also, additional diagnostic quantities can be calculated, such as absolute angular momentum and inertial stability. Asymmetric fields will also be calculated and composited. The asymmetry amplitude can be composited easily, but the asymmetry phase will be more challenging. One possibility to accomplish this compositing is to normalize by asymmetry phase. Also, inner-core hodographs and vertical shear calculations will be made. Finally, additional observational datasets will be added to these composites. In particular, the addition of GPS dropsonde data to the composites will allow a determination of the composite thermodynamic structures in these TCs, especially in the boundary layer.

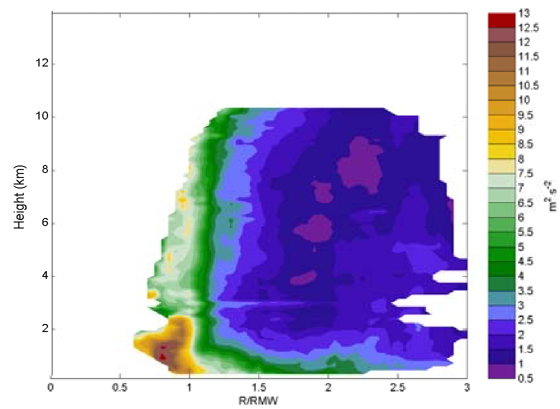

Figure 10. Composite of turbulent kinetic energy calculated from profile data.

There are many possible applications for this compositing methodology. For example, composites of systems exhibiting similar characteristics, such as subsequent rapid intensification(RI)/non-intensification or encounters with vertical shear of different magnitudes and directions can be calculated. Preliminary comparisons of composites of TCs that underwent RI with those that remained steady-state show some key differences in the vortex- and convective-scale structures. Doppler composites can also be used to evaluate model composites from simulations using variable horizontal/vertical resolution or physical parameterizations. All of these activities are currently underway at HRD.

5. REFERENCES

Black, M.L., R.W. Burpee, and F.D. Marks Jr., 1996: Vertical Motion Characteristics of Tropical Cyclones Determined with Airborne Doppler Radial Velocities. *J. Atmos. Sci*., **53**, 1887-1909

Dodge, P., R. W. Burpee, and F. D. Marks Jr., 1999: The Kinematic Structure of a Hurricane with Sea Level Pressure Less Than 900 mb. *Mon. Wea. Rev*., **127**, 987-1004.

Frank, W.M., 1984: A Composite Analysis of the Core of a Mature Hurricane. *Mon. Wea. Rev*. **112**, 2401-2420

Franklin, J.L., M.L. Black, and K. Valde, 2003: GPS Dropwindsonde Wind Profiles in Hurricanes and Their Operational Implications. *Wea. and For*., **18**, 32-44

Gamache, J. F., 1997: Evaluation of a fully three-dimensional variational Doppler analysis technique. Preprints, 28th Conf. on Radar Meteorology, Austin, TX, Amer. Meteor. Soc., 422– 423.

Gamache, J.F., R. A. Houze Jr., and F. D. Marks Jr., 1993: Dual-Aircraft Investigation of the inner Core of Hurricane Norbert. Part III: Water Budget. J. Atmos. Sci., **50**, 3221-3243.

Gao, J., M. Xue, A. Shapiro, and K.K. Droegemeier, 1999: A Variational Method for the Analysis of Three-Dimensional Wind Fields from Two Doppler Radars. *Mon. Wea. Rev*. **127**, 2128-2142

Gray, W.M. and D.J. Shea, 1973: The Hurricane's Inner Core Region. II. Thermal Stability and Dynamic Characteristics. *J. Atmos. Sci*. **30**, 1565-1576.

Houze, R.A., Jr. and F.D. Marks, Jr., 1992: Dual-Aircraft Investigation of the Inner Core of Hurricane Norbert. Part II: Mesoscale Distribution of Ice Particles. *J. Atmos. Sci.*, **49**, 943-963.

Jorgensen, D.P., 1984: Mesoscale and Convective-scale Characteristics of Mature Hurricanes. Part I: General Observations by Research Aircraft. *J. Atmos. Sci*., **41**, 1268-1286.

Kossin, J.P. and M.D. Eastin, 2001: Two Distinct Regimes in the Kinematic and Thermodynamic Structure of the Hurricane Eye and Eyewall. *J. Atmos. Sci.* **58**, 1079-1090

Lee, W.-C. and F. D. Marks, Jr, 2000: Tropical Cyclone Kinematic Structure Retrieved from Single-Doppler Radar Observations. Part II: The GBVTD-Simplex Center Finding Algorithm. *Mon. Wea. Rev*. **128**, 1925-1936

Lorsolo, S., J. Zhang, F.D.Marks, Jr., and J. Gamache, 2010: Estimation and Mapping of Hurricane Turbulent Energy Using Airborne Doppler Measurements, *Mon. Wea. Rev.*, In press.

Marks, F.D., Jr. and R.A. Houze, Jr., 1987: Inner Core Structure of Hurricane Alicia from Airborne Doppler Radar Observations. *J. Atmos. Sci.*, **44**, 1296-1317.

Marks, F.D., Jr., R. A. Houze Jr., J. F. Gamache, 1992: Dual-Aircraft Investigation of the Inner Core of Hurricane Norbert. Part I: Kinematic Structure. *J. Atmos. Sci*. **49**, 919-942

Reasor, P.D., M.D. Eastin, and J.F. Gamache, 2009: Rapidly Intensifying Hurricane Guillermo (1997). Part I: Low-Wavenumber Structure and Evolution. *Mon. Wea. Rev.*, **137**, 603-631

Reasor, P.D., M.T. Montgomery, and L.F. Bosart, 2005: Mesoscale Observations of the Genesis of Hurricane Dolly (1996). *J. Atmos. Sci*. **62**, 3151-3171

Reasor, P.D., M.T. Montgomery, F.D. Marks, Jr., and J.F. Gamache, 2000: Low-Wavenumber Structure and Evolution of the Hurricane Inner Core Observed by Airborne Dual-Doppler Radar. *Mon. Wea. Rev*., **128**, 1653-1680.

Rogers, R.F., S.S. Chen, J. Tenerelli, and H.E. Willoughby, 2003: A Numerical Study of the Impact of Vertical Shear on the Distribution of Rainfall in Hurricane Bonnie (1998). *Mon. Wea. Rev*. **131**, 1577-1599

Shea, D.J. and W.M. Gray, 1973: The Hurricane's Inner Core Region. I. Symmetric and Asymmetric Structure. *J. Atmos. Sci*. **30**, 1544-1564.

Stern, D.P. and D.S. Nolan, 2009: Reexamining the Vertical Structure of Tangential Winds in Tropical Cyclones: Observations and Theory. *J. Atmos. Sci*., **66**, 3579-3600

Yuter, S.E. and R.A. Houze Jr., 1995: Three-Dimensional Kinematic and Microphysical Evolution of Florida Cumulonimbus. Part II: Frequency Distributions of Vertical Velocity, Reflectivity, and Differential Reflectivity. *Mon. Wea. Rev*., **123**, 1941-1963